$G\alpha_{q/11}$ signaling counteracts endothelial dysfunction in the brain and protects cognition in aged mice

Dimitrios Spyropoulos[1,2], Dorothea Ziemens[1,2], Géza Adam Curley[1], Anne-Sophie Gutt[1], Ákos Menyhárt[3,4], Jan Sedlacik[5], Peter Ludewig[6], Jens Fiehler[5], Gereon Hüttmann[7,8], Thomas Andrew Longden[9], Ruben Nogueiras[10], Vincent Prevot[11], Stefan Offermanns[12], Eszter Farkas[3,4], Markus Schwaninger[1,2], and Jan Wenzel[1,2]

[1] Institute of Experimental and Clinical Pharmacology and Toxicology, Center of Brain, Behavior and Metabolism (CBBM), University of Lübeck, Lübeck, Germany

[2] German Research Centre for Cardiovascular Research (DZHK), Hamburg-Lübeck-Kiel, Germany

[3] Hungarian Centre of Excellence for Molecular Medicine – University of Szeged, Cerebral Blood Flow and Metabolism Research Group, Szeged, Hungary

[4] Department of Cell Biology and Molecular Medicine, Albert Szent-Györgyi Medical School and Faculty of Science and Informatics, University of Szeged; Szeged, Hungary

[5] Department of Diagnostic and Interventional Neuroradiology, University Medical Center Hamburg-Eppendorf, Hamburg, Germany

[6] Department of Neurology, University Medical Center Hamburg-Eppendorf, Hamburg, Germany

[7] Institute of Biomedical Optics, University of Lübeck, Lübeck, Germany

[8] German Center of Lung Research (DZL), Gießen, Germany

[9] Department of Physiology, School of Medicine, University of Maryland, Baltimore, USA

[10] Department of Physiology, CIMUS, University of Santiago de Compostela-Instituto de Investigación Sanitaria, Santiago de Compostela, Spain

[11] University of Lille, Inserm, CHU Lille, Laboratory of Development and Plasticity of the Neuroendocrine Brain, Lille Neuroscience & Cognition, UMR-S 1172, DISTALZ, EGID, Lille, France.

[12] Department of Pharmacology, Max Planck Institute for Heart and Lung Research, Bad Nauheim, Germany

Corresponding author:

Jan Wenzel

Institute of Experimental and Clinical Pharmacology and Toxicology, Center of Brain, Behavior and Metabolism (CBBM), University of Lübeck, Ratzeburger Allee 160, 23562 Lübeck, Germany

(+49) 451-3101-7224

Jan.wenzel@uni-luebeck.de

Conflict of interest:

The authors hereby declare that there is no conflict of interest.

43 INTRODUCTORY PARAGRAPH

44 Cognitive impairment is a major medical problem in the aging population. The risk of
45 developing cognitive impairment is higher in several systemic conditions like hypertension,
46 diabetes, and obesity[1-3]. While a vascular contribution to cognitive impairment in these
47 pathologies is well established, the underlying mechanisms are not fully understood[4].
48 Endothelial dysfunction, which frequently accompanies the abovementioned conditions and
49 increases with age[5-7], might be a key causal and mechanistic factor in cognitive deficits
50 associated with systemic conditions.

51 In this study, we demonstrate that the inducible deletion of the $G\alpha_{q/11}$ signaling pathway in
52 brain endothelial cells leads to an impaired reactivity of the brain vasculature to vasodilating
53 stimuli such as neuronal activity, representing an isolated cerebral endothelial dysfunction.
54 These mice develop mild cognitive impairment with aging that could be explained by
55 increased tau phosphorylation, decreased myelination, and capillary rarefaction, suggesting
56 that endothelial cell-driven processes protect cognition in aging and providing a mechanistic
57 explanation for how endothelial dysfunction can lead to cognitive impairment in cerebral
58 small vessel disease.

59 MAIN TEXT

60 Vascular impairment in the central nervous system is implicated in the development of
61 cognitive dysfunction in the elderly, and several systemic diseases are associated with an
62 increased risk of cognitive and vascular deficits[4,6]. Cerebral small vessel disease (cSVD) is
63 considered to be a leading cause of dementia and lacunar stroke[8,9], but the mechanistic role
64 of endothelial dysfunction in this pathology remains unclear.

65 The cerebral vasculature responds to short-term stimuli such as neuronal activity, carbon
66 dioxide, or acute changes in blood pressure through vasodilation or constriction[10]. In addition,
67 a long-term adaptation of the vasculature occurs in pathological conditions like hypertension,
68 diabetes, and obesity[11-13]. Vascular dementia, a severe form of cognitive impairment, is
69 strongly associated with hypertension and cSVD, and it may also be caused by specific
70 mutations in genes affecting vessel composition, such as *NOTCH3* or *COL4A1*[4]. Maladaptation
71 of the cerebral vasculature to underlying diseases may be involved in the development of
72 cognitive dysfunction, and cSVD is especially associated with white matter alterations[4,14,15],
73 early markers in aging-related cognitive decline. Here, we sought to develop a mouse model
74 of cerebral endothelial dysfunction that is not caused by an underlying pathological condition,
75 in order to test the hypothesis that a dysfunctional brain endothelium could cause cSVD and
76 cognitive dysfunction.

77 The endothelial $G\alpha_{q/11}$ signaling pathway is involved in sensing several blood-borne cues in
78 the peripheral vasculature, including shear stress[16]. The deletion of this pathway in all
79 endothelial cells results in hypertension[16], whereas deletion only in the brain endothelium
80 does not alter systemic blood pressure[17]. Several factors, such as thrombin and
81 prostaglandins, act on endothelial receptors that are coupled to $G\alpha_{q/11}$ proteins. However, it
82 is unclear whether this signaling is protective or contributes to age-related deterioration.

83 The cerebral vasculature and especially capillary endothelial cells undergo profound changes
84 during aging[18,19], which are partially reversed by young plasma exposure[18], suggesting an
85 altered role of sensing and transducing mechanisms in brain endothelial cells. The acute
86 response to vasodilatory stimuli reflects the ability of the vasculature to change perfusion and
87 supply oxygen and nutrients, and is strongly impaired in endothelial dysfunction.
88 In order to ascertain the function of the endothelial $G\alpha_{q/11}$ pathway in cerebrovascular
89 vasodilation, we exposed mice lacking $G\alpha_{11}$ and $G\alpha_q$ specifically in the brain endothelium
90 ($G\alpha_{q/11}^{beKO}$) to carbon dioxide (CO_2). As previously demonstrated[17], the acute responsiveness
91 to CO_2 was significantly reduced (Fig. 1A-C). Additionally, mice lacking the endothelial $G\alpha_{q/11}$
92 pathway in the brain exhibited an impaired vascular response to neuronal activity induced by
93 whisker pad stimulation (Fig. 1D-F). In comparable experiments, we did not observe any
94 difference in neuronal activity as measured by local field potentials (Fig. 1G and H), thus
95 confirming an acute endothelium-mediated mechanism acting downstream of neuronal
96 activity.
97 The genetic strategy used to induce the deletion of the $G\alpha_{q/11}$ signaling pathway in brain
98 endothelial cells involves the whole-genome deletion of *Gna11* and the inducible deletion of
99 *Gnaq* using the brain endothelial-specific driver mouse line *Slco1c1*-CreER^{T2} [20]. In *Gna11*
100 knockout mice, the neurovascular coupling response was similar to that in control mice
101 (Extended Fig. 1A and B), indicating that whole-genome deletion of $G\alpha_{11}$ alone does not
102 interfere with neurovascular coupling. Additionally, as *Slco1c1*-CreER^{T2} mice show some minor
103 recombination in astrocytes[20], we also assessed the neurovascular coupling response in
104 astrocyte-specific $G\alpha_{q/11}$ knockout mice using a Glast-CreER^{T2} mouse line[21]. In these mice, the
105 perfusion response to whisker pad stimulation was similar to that in control mice (Extended
106 Fig. 1C and D), supporting the finding that the early phase of vasodilatory responses to

107 neuronal stimulation is not mediated by intracellular calcium release via $G\alpha_{q/11}$-IP_3R signaling
108 in astrocytes[22]. However, prolonged stimulation might have produced different results since
109 astrocytic calcium is involved in the later, sustained phase of neurovascular coupling[23].
110 Brain endothelial $G\alpha_{q/11}$ proteins have been shown to affect ion channel activities, some of
111 which affect neurovascular coupling responses[24-26]. Nevertheless, it is still not yet clear
112 whether endothelial $G\alpha_{q/11}$ proteins themselves are involved in the vasodilation upon
113 neuronal activity. To validate our findings, we repeated the experiments in a different
114 laboratory environment using alternative anesthesia and without artificially ventilating the
115 mice. Consistent with the former results, we found that $G\alpha_{q/11}^{beKO}$ mice exhibited a reduced
116 perfusion response compared to control mice (Fig. 1I and J). In summary, the vascular
117 response to neuronal activity or carbon dioxide is strongly impaired in $G\alpha_{q/11}^{beKO}$ mice
118 indicating a cerebral endothelial dysfunction similar to the human situation in cSVD[4,9].
119 Functional impairment of the brain´s vasculature may be accompanied or even caused by
120 morphological alterations of the vessel structure. Previously, we demonstrated that the
121 endothelial cells of the main arteries in the brain show recombination in *Slco1c1*-$CreER^{T2}$
122 mice[27]. Tissue sections from the head-supplying arteries using the reporter mouse line
123 *Slco1c1*-$CreER^{T2}$;$Ai14^{+/fl}$ [28] confirmed that the recombination leading to tdTomato expression
124 in this mouse line affected the internal carotid artery starting from the bifurcation but not the
125 external carotid artery (Extended Fig. 2). We next sought to determine whether changes in
126 brain-supplying vessels brought about functional impairment in $G\alpha_{q/11}^{beKO}$ mice and used two
127 techniques – time-of-flight (TOF) angiography and two-photon microscopy – to trace the
128 vasculature from the arterial level down to the capillary level in living mice.
129 The three-dimensional reconstruction of TOF angiography (Fig. 2A, Extended Fig. 3) and
130 analyses of two main arterial vascular trees, namely the middle and the posterior cerebral

131 artery (MCA and PCA, respectively), revealed no major differences in terms of diameter,
132 overall volume, or straightness between control and $G\alpha_{q/11}^{beKO}$ mice (Fig. 2A-H), although the
133 PCA and its branches in $G\alpha_{q/11}^{beKO}$ mice showed a little reduction in straightness and had
134 slightly higher volumes than those in control mice (Fig. 2F, H). However, this technique has a
135 limited spatial resolution and only detects large arteries and arterioles on the surface of the
136 brain. As vascular resistance and flow regulation are primarily mediated by smaller arterioles
137 and first-order capillaries[10], we used two-photon microscopy to examine the vasculature in
138 greater detail (Fig. 2I). We recorded volumes of the cortical vasculature along entire vascular
139 trees (Fig. 2I, left panel) as well as fast line scans along individual vessels to calculate blood
140 flow velocity (Fig. 2I, right panels). No differences were found between control and $G\alpha_{q/11}^{beKO}$
141 mice in terms of arteriolar or capillary diameter (Fig. 2J, L), or red blood cell speed (Fig. 2M),
142 thus extending the TOF-angiography results to smaller blood-supplying vessels. Interestingly,
143 the diameter of venules was smaller in $G\alpha_{q/11}^{beKO}$ compared to control mice (Fig. 2K) without
144 affecting the RBC velocity (Fig. 2M), suggesting an impairment of the passive venular part of
145 the vascular tree and might hint at an impaired blood drainage. Finally, we used arterial spin
146 labeling MRI to determine whether these small vascular alterations affected overall perfusion
147 in several brain regions; however, we found no differences between $G\alpha_{q/11}^{beKO}$ and control
148 mice (Fig. 2N and O).
149 Endothelial dysfunction is a feature of cSVD, which is linked to cognitive impairment[14,29,30].
150 $G\alpha_{q/11}^{beKO}$ mice offer an opportunity to investigate the cognitive consequences of an isolated
151 functional impairment of the brain endothelium in the absence of an underlying pathological
152 condition. To test memory, we performed object-place recognition tests (Fig. 3A) before
153 inducing the knockout at eight weeks of age (Fig. 3B) and at various time points subsequently
154 during the lifespan of the same mice (Fig. 3C-E). Interestingly, only $G\alpha_{q/11}^{beKO}$ mice at the age

155 of 18 months failed to reach a significant preference for the replaced object, indicating a mild
156 cognitive deficit (Fig. 3E). To further investigate memory function in these old mice, we
157 performed a Barnes maze test when they were 20-22 months old (Fig. 3F). During the learning
158 phase of the test, control mice displayed the expected improvement in their search strategy
159 with the most of the single tests being solved by directly finding the hole on day five (Fig. 3G
160 and I). $G\alpha_{q/11}^{beKO}$ mice, in contrast, had a marked improvement from day one to day two of
161 the learning phase but failed to improve further in subsequent days (Fig. 3H). On day five, they
162 utilized significantly fewer direct strategies to find the hole than the control mice did (Fig. 3I).
163 Also, the primary latency, until the hole was found, was higher in $G\alpha_{q/11}^{beKO}$ mice throughout
164 almost the whole learning phase (Fig. 3J). Lastly, on the test days, $G\alpha_{q/11}^{beKO}$ mice performed
165 worse than control mice, showing a significantly higher number of primary errors and latency
166 on day six, but not on day 17 (Fig. 3K and L), indicating mild cognitive deficits and prolonged
167 duration of memory retrieval.
168 It has been recently shown that cerebral endothelial dysfunction induced by high dietary salt
169 gives rise to increased tau phosphorylation due to reduced nitric oxide (NO) release, leading
170 to cognitive impairment[31]. Hyperphosphorylation of tau is a hallmark of certain
171 neurodegenerative diseases and causes cognitive impairment via neuronal dysfunction[32]. NO
172 release is strongly induced by the activation of endothelial $G\alpha_{q/11}$ signaling, which activates
173 the endothelial NO synthase, and this could provide a link between cerebrovascular and
174 cognitive dysfunction in $G\alpha_{q/11}^{beKO}$ mice. Therefore, we measured tau phosphorylation in the
175 hippocampus and cortex of $G\alpha_{q/11}^{beKO}$ and control mice. We found increased phosphorylation
176 (Fig. 3M and Extended Fig. 4A-C) at epitopes that promote tau aggregation and neuronal
177 dysfunction (pSer202/pThr205 by AT8 and pThr231 by AT180 antibodies)[32].
178 Immunofluorescence staining of neuronal and synaptic markers showed that the number of

179 neurons and synapses in the hippocampus and cortex of aged $G\alpha_{q/11}^{beKO}$ mice was unchanged
180 (Extended Fig. 5 and Extended Fig. 6A and B), indicating normal cellular morphology and a
181 functional deficit in these brain regions rather than a morphological one. In addition, the
182 expression of brain-derived neurotrophic factor (BDNF), a neuroprotective protein[33] whose
183 presence in endothelial cells is essential for memory function[34], was not altered in cortical and
184 hippocampal tissue of aged $G\alpha_{q/11}^{beKO}$ mice as well (Extended Fig. 6C and D). However, early
185 markers of vascular dementia in humans include white matter alterations with increased
186 hyperintensities indicating disturbed myelination[4,14]. Therefore, we examined the myelination
187 levels by staining for myelin basic protein (MBP) in grey and white matter areas in different
188 regions along the mouse brain (Fig. 4A-D). We found decreased myelination in the posterior
189 part of the forebrain, which was most prominent in the white matter of the corpus callosum
190 (Fig. 4C and D). Together with increased tau phosphorylation, this finding suggests that brain
191 endothelial $G\alpha_{q/11}$ signaling protects against neuronal dysfunction in aged mice. Interestingly,
192 we observed no signs of neuroinflammation in different brain regions of aged $G\alpha_{q/11}^{beKO}$ mice
193 when stained for microglia and astrocytic activation (Extended Fig. 6E-I).
194 The cognitive impairment in old $G\alpha_{q/11}^{beKO}$ mice has an endothelial origin. Therefore, we
195 investigated the vessel structure of these mice by staining. Indeed, we found an increased
196 level of so-called string vessels – empty basement membrane tubes that indicate endothelial
197 cell death[35] – in all the areas we investigated in aged but not adult $G\alpha_{q/11}^{beKO}$ mice (Fig. 4E and
198 F, Extended Fig. 7A-C). The increase in string vessels was most apparent in the corpus callosum
199 and it was accompanied by a decrease in vessel density in this region (Fig. 4F and G). This is
200 notable given that the corpus callosum has a lower vascular density than the cortex and
201 hippocampus (Fig. 4G, Extended Fig. 7D), and it may explain the decreased myelination in this
202 region in $G\alpha_{q/11}^{beKO}$ mice since small vessels are discussed to contribute to white matter

203 changes in aging[36]. In addition to the vascular deficit, we also found a slight increase in BBB
204 permeability in the hippocampus but not the cortex, measured by albumin content in brain
205 tissue of aged perfused $G\alpha_{q/11}^{beKO}$ mice (Fig. 4H). $G\alpha_{q/11}$ signaling in endothelial cells is related
206 not only to NO release but also to signaling by VEGF, a vasoprotective agent[37]. The loss of
207 endothelial cells in the brain might be caused by reduced VEGF signaling although we did not
208 observe any differences in plasma VEGF levels between control and $G\alpha_{q/11}^{beKO}$ mice (Extended
209 Fig. 7E). However, the protein levels of the main VEGF receptor downstream of $G\alpha_{q/11}$
210 signaling, $VEGFR_2$, were reduced in the brains of aged $G\alpha_{q/11}^{beKO}$ mice (Fig. 4I). Since many
211 regressing blood vessels in the brain were recently shown to regrow again[38], an impaired
212 $VEGFR_2$-related vessel proliferation might contribute to the increased occurrence of string
213 vessels in those mice. Disturbed vascularization and impaired VEGF signaling in the whole
214 body are strongly correlated with a decreased lifespan[39]. If the brain plays an essential role in
215 determining life expectancy, this effect could help explain the increased mortality rate
216 observed in $G\alpha_{q/11}^{beKO}$ mice in the course of aging (Extended Fig. 7F).
217 In summary, we present a mouse model of an inducible and isolated cerebral endothelial
218 dysfunction that leads to an impaired cerebrovascular reactivity to CO_2 and neuronal activity
219 in adult mice. As they age, these mice develop some mild cognitive impairment, indicating a
220 causal relationship between endothelial dysfunction and cognitive deficits. While many
221 diseases lead to endothelial dysfunction and cognitive deficits, it is unclear whether
222 endothelial dysfunction itself contributes to impaired brain function. Here, we show that
223 reduced endothelial GPCR signaling and vascular reactivity result in increased tau
224 phosphorylation in the cortex and the hippocampus. This effect could be explained by reduced
225 NO release from endothelial cells as demonstrated previously in primary cells of this mouse
226 line[17]. Endothelium-derived mediators such as NO and VEGF affect not only the vasculature

227 but are also essential for neuronal function[40]. Reduced expression of $VEGFR_2$ in the brains of
228 these mice suggests a local imbalance of factors affecting vascular as well as neuron-mediated
229 functions. Based on neuronal and synaptic markers, we demonstrate that neurons of
230 $G\alpha_{q/11}^{beKO}$ mice are not morphologically but functionally impaired, leading to reduced memory
231 retrieval in aged mice. The combination of old age and impaired cerebrovascular reactivity
232 leads to an increased occurrence of string vessels in various regions and capillary rarefaction
233 in the white matter of the brain. String vessels due to the loss of endothelial $G\alpha_{q/11}$ signaling
234 were most prevalent in the white matter of the brain in aged mice, suggesting that these areas
235 are particularly susceptible to vascular dysfunction. The reduced myelin content may partially
236 explain the memory impairment in these mice, since a similar phenomenon is discussed to
237 contribute to cognitive impairment in patients with small vessel disease[41], and loss of white
238 matter during aging contributes to cognitive decline[42]. Interestingly, the white matter is
239 severely affected in cerebral small vessel diseases[4,43], and string vessels are a feature of other
240 models of cerebral small vessel diseases as well[27,44,45]. Increased mortality in $G\alpha_{q/11}^{beKO}$ mice
241 during aging may be explained by vascular rarefaction and increased blood-brain barrier
242 permeability, which could lead to epileptic seizures or ischemic events. $VEGFR_2$ expression
243 was reduced in aged $G\alpha_{q/11}^{beKO}$ mice, which may be critical for the development of string
244 vessels, as it has been shown to mediate the survival of physiologically obstructed capillaries
245 and thereby prevent pruning[46].
246 $G\alpha_{q/11}^{beKO}$ mice provide a new model for investigating age-induced and endothelium-
247 mediated cognitive impairment, making them ideal for exploring the mechanisms and targets
248 of neurovascular dysfunction prevention in the elderly. We identified the endothelial $G\alpha_{q/11}$
249 signaling pathway as a protective mechanism for cerebrovascular reactivity and the aging
250 vasculature in the brain. Microvascular targeting in endothelial dysfunction could counteract

251 age-related neurological disorders, as demonstrated by blood-brain barrier-stabilizing
252 approaches[47,48] or by VEGF administration[39]. In this study, we present endothelial $G\alpha_{q/11}$
253 signaling as an additional protective pathway that should be maintained and could be targeted
254 in cerebrovascular dysfunction.
255

256 ACKNOWLEDGMENTS

257 We would like to thank Beate Lembrich and Ines Stölting (University of Lübeck, Germany) for
258 their expert technical assistance. We also thank Sonja Binder (University of Lübeck, Germany)
259 for support with behavioral tests. This research was supported by grants from the European
260 Research Council (Synergy grant no. 2019-WATCH-810331 to R.N., V.P., and M.S.), the
261 Deutsche Forschungsgemeinschaft (SCHW 416/12-1 to M.S.; WE 6456/1-1 to J.W.; GRK1957
262 to M.S. and J.W.), and the Marie Skłodowska-Curie European Union's Horizon 2020 research
263 and innovation program (no. 813294 (ENTRAIN) to M.S. and J.W.). Graphical inlets were
264 created with BioRender.com.
265

266 REFERENCES

267 1 Jones, A. *et al.* Potentially modifiable risk factors for dementia and mild cognitive
268 impairment: an umbrella review and meta-analysis. *Dement Geriatr Cogn Disord* **53**,
269 91-106, doi:10.1159/000536643 (2024).
270 2 Iadecola, C. & Gottesman, R. F. Neurovascular and cognitive dysfunction in
271 hypertension. *Circulation research* **124**, 1025-1044,
272 doi:10.1161/CIRCRESAHA.118.313260 (2019).
273 3 Frankel D S, M. J. B., Massaro J M, Wilson P W F , O'Donnell C J, D'Agostino R B, Tofler
274 G H. Von Willebrand factor, type 2 diabetes mellitus, and risk of cardiovascular
275 disease: the framingham offspring study. *Circulation* **118**, 2533-2539,
276 doi:10.1161/CIRCULATIONAHA.108.792986. (2008).
277 4 Markus, H. S. & Joutel, A. The pathogenesis of cerebral small vessel diseases and
278 vascular cognitive impairment. *Physiological reviews*,
279 doi:10.1152/physrev.00028.2024 (2025).
280 5 Yang, T., Sun, Y., Lu, Z., Leak, R. K. & Zhang, F. The impact of cerebrovascular aging on
281 vascular cognitive impairment and dementia. *Ageing Res Rev* **34**, 15-29,
282 doi:10.1016/j.arr.2016.09.007 (2017).

6 Li, T. *et al.* Age-related cerebral small vessel disease and inflammaging. *Cell Death Dis* **11**, 932, doi:10.1038/s41419-020-03137-x (2020).
7 Virdis A, M. S., Colucci R, Chiriacò M, Uliana M, Puxeddu I, Bernardini N, Blandizzi C, Taddei S, . Microvascular endothelial dysfunction in patients with obesity. *Current Hypertension Reports* **21**, doi:10.1007/s11906-019-0930-2 (2019).
8 Debette, S., Schilling, S., Duperron, M. G., Larsson, S. C. & Markus, H. S. Clinical significance of magnetic resonance imaging markers of vascular brain injury: a systematic review and meta-analysis. *JAMA Neurol* **76**, 81-94, doi:10.1001/jamaneurol.2018.3122 (2019).
9 Kremer, R., Williams, A. & Wardlaw, J. Endothelial cells as key players in cerebral small vessel disease. *Nature reviews. Neuroscience* **26**, 179-188, doi:10.1038/s41583-024-00892-0 (2025).
10 Schaeffer, S. & Iadecola, C. Revisiting the neurovascular unit. *Nature neuroscience* **24**, 1198-1209, doi:10.1038/s41593-021-00904-7 (2021).
11 Letra L., S. C. Cerebrovascular Disease: Consequences of obesity-induced endothelial dysfunction. *Advances in Neurobiology*, doi:10.1007/978-3-319-63260-5_7. (2017).
12 Santisteban, M. M., Iadecola, C. & Carnevale, D. Hypertension, neurovascular dysfunction, and cognitive Impairment. *Hypertension* **80**, 22-34, doi:10.1161/HYPERTENSIONAHA.122.18085 (2023).
13 Horton, W. B. & Barrett, E. J. Microvascular dysfunction in diabetes mellitus and cardiometabolic disease. *Endocrine reviews* **42**, 29-55, doi:10.1210/endrev/bnaa025 (2021).
14 Vlegels, N. *et al.* The relation between cerebral small vessel function and white matter microstructure in monogenic and sporadic small vessel disease - the ZOOM@SVDs study. *Cereb Circ Cogn Behav* **8**, 100383, doi:10.1016/j.cccb.2025.100383 (2025).
15 Wang, S. *et al.* Superficial white matter microstructure affects processing speed in cerebral small vessel disease. *Hum Brain Mapp* **43**, 5310-5325, doi:10.1002/hbm.26004 (2022).
16 Wang, S. *et al.* P2Y(2) and Gq/G(1)(1) control blood pressure by mediating endothelial mechanotransduction. *The Journal of clinical investigation* **125**, 3077-3086, doi:10.1172/JCI81067 (2015).
17 Wenzel, J. *et al.* Impaired endothelium-mediated cerebrovascular reactivity promotes anxiety and respiration disorders in mice. *Proceedings of the National Academy of Sciences of the United States of America* **117**, 1753-1761, doi:10.1073/pnas.1907467117 (2020).
18 Chen, M. B. *et al.* Brain endothelial cells are exquisite sensors of age-related circulatory cues. *Cell reports* **30**, 4418-4432 e4414, doi:10.1016/j.celrep.2020.03.012 (2020).
19 Bennett, H. C. *et al.* Aging drives cerebrovascular network remodeling and functional changes in the mouse brain. *Nature communications* **15**, 6398, doi:10.1038/s41467-024-50559-8 (2024).
20 Ridder, D. A. *et al.* TAK1 in brain endothelial cells mediates fever and lethargy. *The Journal of experimental medicine* **208**, 2615-2623, doi:10.1084/jem.20110398 (2011).
21 Mori, T. *et al.* Inducible gene deletion in astroglia and radial glia--a valuable tool for functional and lineage analysis. *Glia* **54**, 21-34, doi:10.1002/glia.20350 (2006).
22 Nizar, K. *et al.* In vivo stimulus-induced vasodilation occurs without IP3 receptor activation and may precede astrocytic calcium increase. *The Journal of neuroscience :*

the official journal of the Society for Neuroscience **33**, 8411-8422, doi:10.1523/JNEUROSCI.3285-12.2013 (2013).

23 Institoris, A. *et al.* Astrocytes amplify neurovascular coupling to sustained activation of neocortex in awake mice. *Nature communications* **13**, 7872, doi:10.1038/s41467-022-35383-2 (2022).

24 Harraz, O. F., Longden, T. A., Dabertrand, F., Hill-Eubanks, D. & Nelson, M. T. Endothelial GqPCR activity controls capillary electrical signaling and brain blood flow through PIP2 depletion. *Proceedings of the National Academy of Sciences of the United States of America* **115**, E3569-E3577, doi:10.1073/pnas.1800201115 (2018).

25 Longden, T. A. *et al.* Local IP(3) receptor-mediated Ca(2+) signals compound to direct blood flow in brain capillaries. *Science advances* **7**, doi:10.1126/sciadv.abh0101 (2021).

26 Mughal, A. *et al.* Electrocalcium coupling in brain capillaries: Rapidly traveling electrical signals ignite local calcium signals. *Proceedings of the National Academy of Sciences of the United States of America* **121**, e2415047121, doi:10.1073/pnas.2415047121 (2024).

27 Ridder, D. A. *et al.* Brain endothelial TAK1 and NEMO safeguard the neurovascular unit. *The Journal of experimental medicine* **212**, 1529-1549, doi:10.1084/jem.20150165 (2015).

28 Madisen, L. *et al.* A robust and high-throughput Cre reporting and characterization system for the whole mouse brain. *Nature neuroscience* **13**, 133-140, doi:10.1038/nn.2467 (2010).

29 de Leeuw, F. E. *et al.* Endothelial cell activation is associated with cerebral white matter lesions in patients with cerebrovascular disease. *Annals of the New York Academy of Sciences* **977**, 306-314, doi:10.1111/j.1749-6632.2002.tb04831.x (2002).

30 Rajani, R. M. *et al.* Reversal of endothelial dysfunction reduces white matter vulnerability in cerebral small vessel disease in rats. *Sci Transl Med* **10**, doi:10.1126/scitranslmed.aam9507 (2018).

31 Faraco, G. *et al.* Dietary salt promotes cognitive impairment through tau phosphorylation. *Nature* **574**, 686-690, doi:10.1038/s41586-019-1688-z (2019).

32 Wang, Y. & Mandelkow, E. Tau in physiology and pathology. *Nature reviews. Neuroscience* **17**, 5-21, doi:10.1038/nrn.2015.1 (2016).

33 Bathina, S. & Das, U. N. Brain-derived neurotrophic factor and its clinical implications. *Arch Med Sci* **11**, 1164-1178, doi:10.5114/aoms.2015.56342 (2015).

34 Quirie, A. *et al.* Anxio-depressive phenotype and impaired memory in mice with a conditional knockout of brain-derived neurotrophic factor in endothelial cells. *Am J Physiol Cell Physiol* **328**, C303-C314, doi:10.1152/ajpcell.00699.2024 (2025).

35 Brown, W. R. A review of string vessels or collapsed, empty basement membrane tubes. *Journal of Alzheimer's disease : JAD* **21**, 725-739, doi:10.3233/JAD-2010-100219 (2010).

36 Salat, D. H. Imaging small vessel-associated white matter changes in aging. *Neuroscience* **276**, 174-186, doi:10.1016/j.neuroscience.2013.11.041 (2014).

37 Sivaraj, K. K. *et al.* Endothelial Galphaq/11 is required for VEGF-induced vascular permeability and angiogenesis. *Cardiovascular research* **108**, 171-180, doi:10.1093/cvr/cvv216 (2015).

38 Gao, X. *et al.* Reduction of neuronal activity mediated by blood-vessel regression in the adult brain. *Nature communications* **16**, 5840, doi:10.1038/s41467-025-60308-0 (2025).

39 Grunewald, M. *et al.* Counteracting age-related VEGF signaling insufficiency promotes healthy aging and extends life span. *Science* **373**, doi:10.1126/science.abc8479 (2021).
40 Aksan, B. & Mauceri, D. Beyond vessels: unraveling the impact of VEGFs on neuronal functions and structure. *J Biomed Sci* **32**, 33, doi:10.1186/s12929-025-01128-8 (2025).
41 Denecke, J. *et al.* Reduced myelin contributes to cognitive impairment in patients with monogenic small vessel disease. *Alzheimer's & dementia : the journal of the Alzheimer's Association* **21**, e70127, doi:10.1002/alz.70127 (2025).
42 Gunning-Dixon, F. M., Brickman, A. M., Cheng, J. C. & Alexopoulos, G. S. Aging of cerebral white matter: a review of MRI findings. *Int J Geriatr Psychiatry* **24**, 109-117, doi:10.1002/gps.2087 (2009).
43 Benisty, S. *et al.* White-matter lesions without lacunar infarcts in CADASIL. *Journal of Alzheimer's disease : JAD* **29**, 903-911, doi:10.3233/JAD-2012-111784 (2012).
44 Muller, K., Courtois, G., Ursini, M. V. & Schwaninger, M. New insight into the pathogenesis of cerebral small-vessel diseases. *Stroke* **48**, 520-527, doi:10.1161/STROKEAHA.116.012888 (2017).
45 Tong, X. K. & Hamel, E. Simvastatin restored vascular reactivity, endothelial function and reduced string vessel pathology in a mouse model of cerebrovascular disease. *Journal of cerebral blood flow and metabolism : official journal of the International Society of Cerebral Blood Flow and Metabolism* **35**, 512-520, doi:10.1038/jcbfm.2014.226 (2015).
46 Reeson, P., Choi, K. & Brown, C. E. VEGF signaling regulates the fate of obstructed capillaries in mouse cortex. *eLife* **7**, doi:10.7554/eLife.33670 (2018).
47 Greene, C. *et al.* Microvascular stabilization via blood-brain barrier regulation prevents seizure activity. *Nature communications* **13**, 2003, doi:10.1038/s41467-022-29657-y (2022).
48 Martin, M. *et al.* Engineered Wnt ligands enable blood-brain barrier repair in neurological disorders. *Science* **375**, eabm4459, doi:10.1126/science.abm4459 (2022).
49 Wettschureck, N. *et al.* Absence of pressure overload induced myocardial hypertrophy after conditional inactivation of Galphaq/Galpha11 in cardiomyocytes. *Nature medicine* **7**, 1236-1240, doi:10.1038/nm1101-1236 (2001).
50 Huber, G. *et al.* Telmisartan prevents high-fat diet-induced neurovascular impairments and reduces anxiety-like behavior. *Journal of cerebral blood flow and metabolism : official journal of the International Society of Cerebral Blood Flow and Metabolism* **41**, 2356-2369, doi:10.1177/0271678X211003497 (2021).
51 Csaszar, E. *et al.* Microglia modulate blood flow, neurovascular coupling, and hypoperfusion via purinergic actions. *The Journal of experimental medicine* **219**, doi:10.1084/jem.20211071 (2022).
52 Luh, W. M., Wong, E. C., Bandettini, P. A. & Hyde, J. S. QUIPSS II with thin-slice TI1 periodic saturation: a method for improving accuracy of quantitative perfusion imaging using pulsed arterial spin labeling. *Magnetic resonance in medicine* **41**, 1246-1254 (1999).
53 Binder, S. *et al.* Sleep enhances memory consolidation in the hippocampus-dependent object-place recognition task in rats. *Neurobiol Learn Mem* **97**, 213-219, doi:10.1016/j.nlm.2011.12.004 (2012).

54 Murai, T., Okuda, S., Tanaka, T. & Ohta, H. Characteristics of object location memory in mice: Behavioral and pharmacological studies. *Physiol Behav* **90**, 116-124, doi:10.1016/j.physbeh.2006.09.013 (2007).

55 Binder, S. *et al.* Monosynaptic hippocampal-prefrontal projections contribute to spatial memory consolidation in mice. *The Journal of neuroscience : the official journal of the Society for Neuroscience* **39**, 6978-6991 (2019).

56 Wenzel, J. *et al.* The SARS-CoV-2 main protease M(pro) causes microvascular brain pathology by cleaving NEMO in brain endothelial cells. *Nature neuroscience* **24**, 1522-1533, doi:10.1038/s41593-021-00926-1 (2021).

436 METHODS

437 *Mice*

438 All the mouse lines were established on a C57BL/6 background. We used littermate mice that
439 were sex- and age-matched between experimental groups. All animal experiments were
440 approved by the local animal ethics committee (Regierungspräsidium Karlsruhe; Ministerium
441 für Landwirtschaft, Umwelt und ländliche Räume, Kiel, Germany). The mice were kept at a
442 constant temperature (22°C) on a 12-hour light/ dark cycle and were provided with standard
443 laboratory chow and water *ad libitum*.

444 Brain endothelial-specific knockout (beKO) animals were generated by using the BAC-
445 transgenic *Slco1c1*-CreER^{T2} strain[20], which expresses the tamoxifen-inducible CreER^{T2}
446 recombinase under the control of the mouse *Slco1c1* regulatory sequences in brain
447 endothelial cells. The Cre mice were crossed with mice carrying a floxed $G\alpha_q$ allele (Gnaq$^{fl/fl}$),
448 and they were $G\alpha_{11}$-deficient (Gna11$^{-/-}$)[49] (Gnaq$^{fl/fl}$::Gna11$^{-/-}$), leading to a deletion of the
449 $G\alpha_{q/11}$ pathway in brain endothelial cells. Littermates lacking the Cre transgene and
450 heterozygous for $G\alpha_{11}$ (Gnaq$^{fl/fl}$::Gna11$^{-/+}$) were used as controls and received tamoxifen in
451 parallel with the knockout animals. To induce the deletion of the $G\alpha_{q/11}$ pathway in astrocytes,
452 we used a Glast-CreER^{T2} mouse line[21], and to assess recombination in the *Slco1c1*-CreER^{T2}
453 strain, we used the Ai14 reporter mouse leading to tdTomato expression upon
454 recombination[28].

455 All animals were injected with 1 mg tamoxifen (Sigma-Aldrich) per 20 g body weight dissolved
456 in 90% miglyol® 812 /10% ethanol i.p. every 12 h for 5 consecutive days. The investigators
457 were blinded to the genotype of the mice in all experiments and analyses.

458

459 *Neurovascular Coupling and CO_2 stimulation - Laser speckle imaging.*

460 The mice were anesthetized with ketamine (70 µg/g body weight, bela-pharm) and xylazine
461 (16 µg/g body weight, Bayer AG). The body temperature was maintained at 37 ± 0.2°C
462 throughout the study using a feedback-regulated warming system (TCAT-2LV, Physitemp
463 Instruments). A small ventilatory tube was inserted into the trachea after tracheotomy was
464 performed and connected to a small animal ventilation device (MiniVent, Harvard Apparatus).
465 The mice were ventilated with a gas mixture reflecting normal air (21 % O_2, 79 % N_2). The
466 ventilation volume was constant, and the ventilation frequency was adjusted to a
467 physiological expiratory CO_2 concentration of 35-45 mmHg that was continuously controlled
468 during the experiments with a capnometer (microCapstar, CWE Inc.). The skin over the head
469 was removed, but the skull remained intact for the whole experiment. Laser speckle imaging
470 (FLPI, Moor instruments) was carried out using a recording rate of 0.25 Hz during CO_2
471 stimulation or 25 Hz to measure neurovascular coupling responses. Regions of interest were
472 defined over the somatosensory cortex (see Fig. 1D), and the flux intensities were normalized
473 to the baseline values. CO_2 stimulation was performed using a gas mixture containing 10 %
474 CO_2, combined with 21 % O_2 and 69 % N_2. To measure neurovascular coupling, the whisker
475 pad was electrically stimulated for five seconds using bipolar pulses (750 µA, 1 ms, 5 Hz;
476 STG4002, Multichannel systems) after inserting two needle electrodes subcutaneously as
477 described before[50]. Stimulation was performed five times, and mean curves of each mouse
478 were analyzed.
479
480 *Neurovascular Coupling - laser Doppler recording*
481 The mice were anesthetized with 1.5–2 % isoflurane in a mixture of 40 % O_2 and 60 % N_2, and
482 were allowed to breathe spontaneously through a head mask. The body temperature was
483 maintained at 37 °C with a servo-controlled heating pad. The animal was fixed in a stereotaxic
484 frame, and a craniotomy was performed in the right parietal bone using a drill. The dura in the

485 cranial window was carefully dissected, and the tissue was kept wet with aCSF (pH 7.4). A laser
486 Doppler needle probe (Periflux 5000, Perimed AB) was positioned at the somatosensory
487 cortex. Neurovascular stimulation was performed as previously described[51]. In brief, whiskers
488 were stimulated electromechanically with a bending actuator (#PL112-PL140; PICMA)
489 connected to a piezo amplifier (#E-650 Amplifier, Physik Instrumente) according to the
490 following protocol: the left whiskers were stimulated for 30 s, repeated 3 times, 60 s apart.
491 Stimulation-evoked perfusion responses in the contralateral cortex were recorded using the
492 laser Doppler probe.
493
494 *Local field potential (LFP) recordings*
495 LFPs were measured as described before[27]. Briefly, mice were prepared in a similar way to
496 that for laser speckle imaging, including anesthesia with ketamine/xylazine and artificial
497 ventilation (see above). Two holes were drilled to place the electrodes (Tungsten
498 microelectrodes; FHC), the first one over the cerebellum for the reference electrode and a
499 second one over the barrel cortex for the recording electrode. The whisker pad was stimulated
500 in a similar way to the neurovascular coupling stimulation described above, using electrodes
501 inserted into the whisker pad and an electrical stimulator. The stimulus was the same as
502 described before, too (see above). LFPs were recorded with an amplifier (Model 1800; AM-
503 Systems) and converted into a digital format by an AD converter (PowerLab 8/30 ML870;
504 ADInstruments). LabChart 7 (ADInstruments) was used to record and analyze the data
505 (sampling rate 20 kHz; notch filter 50 Hz). For each mouse, four to six different areas in the
506 contralateral barrel cortex were recorded to find the region with the highest response upon
507 whisker stimulation. Here, each region was stimulated three times. Then the amplitudes of 30
508 pulses taken from the region having the highest amplitude were averaged for each mouse.

509

510 *Arterial Spin labeling MRI measurements*

511 Anesthesia was induced by 4 % and maintained at ~0.8-1 % isoflurane in 21 % O_2 and 79 % N_2.
512 The respiration rate and body temperature were continuously monitored using an MRI-
513 compatible system, and the temperature was maintained at 37 ± 0.2°C throughout the study
514 using a feedback-regulated warming system (Small Animal Instruments Inc.). The mice were
515 scanned using a 7 Tesla small animal MRI scanner (ClinScan, Bruker) with a ^{1}H receive-only 2x2
516 mouse brain surface array coil. The array coil was placed closely to the neck and back of the
517 head. Anatomical image data were acquired using a T2-weighted turbo spin-echo sequence
518 with the following sequence parameters: echo time – TE = 65 ms, repetition time – TR = 3000
519 ms, field of view – FoV = 16×16 mm^2, image matrix = 192×192, turbo factor = 9, number of
520 slices = 15, slice thickness = 0.5 mm, readout bandwidth = 100 Hz/pixel, 50 % phase
521 oversampling, and total acquisition time = 3:15 min. CBF was measured by arterial spin
522 labeling (ASL) with Q2TIPS (quantitative imaging of perfusion using a single subtraction with
523 interleaved thin-slice TI1 periodic saturation)[52] with TI1/TI2/SS = 900/1400/1375 ms and with
524 45 control-label pairs. Other ASL scanning parameters were: Echo planar imaging technique
525 with TE =7.3 ms, TR =3000 ms, FoV =16×16 mm^2, image matrix = 64×64, number of slices = 3,
526 slice thickness = 0.5 mm, partial Fourier factor =6/8, readout bandwidth = 4340 Hz/pixel, and
527 total acquisition time = 4:38 min.

528

529 *Time-of-Flight (TOF) MR angiography*

530 Time-of-Flight (TOF) MR angiography was performed during the same imaging session as
531 follows: TE = 3.06 ms, TR = 18 ms, FoV = 20×20 mm^2, image matrix = 256×256, partial Fourier
532 factor in phase encoding direction = 6/8, number of imaging slabs = 4, number of slices per

533 slab = 28, slab overlap = 18%, slice thickness = 0.13 mm, readout bandwidth = 151 Hz/pixel,
534 total acquisition time = 6:24 min. The voxel size of the data sets was 78 x 78 x 51 µm.
535 For analyses of the cerebral arterial vasculature, the TOF data sets were analyzed using IMARIS
536 (v9.9.1, Bitplane) as illustrated in Extended Fig. 3. An autopath tracing algorithm was used for
537 the analysis of the middle cerebral artery (MCA) and posterior cerebral artery (PCA) of the left
538 and right hemispheres. In brief, we used the surface creation feature of the software, followed
539 by an automatic thresholding adjustment to subtract background signals, and a manual
540 deletion of signals that were not part of the cerebral artery network. A mask of the final
541 surface was created, and the filament tracing tool of the software was used to generate an
542 autopath. To analyze only the vessel structure of the MCAs and PCAs, the starting points were
543 set to the diverging points at the Circle of Willis. The mean diameter, the volumes, and the
544 straightness were measured in all detectable branches of the traced MCAs and PCAs and
545 averaged for each animal.
546
547 *Two-photon microscopy*
548 Mice were anesthetized with urethane (1.8 – 2.0 mg/g body weight), tracheotomized, and
549 artificially ventilated (79 % N_2, 21 % O_2; MiniVent, Hugo Sachs Elektronik). The ventilation
550 volume was constant, and the ventilation frequency was adjusted to a physiological expiratory
551 CO_2 concentration of 35-45 mmHg that was continuously controlled during the experiments
552 with a capnometer (microCapstar, CWE Inc.). Tetramethylrhodamine B thiocarbamoyl (TRITC)
553 dextran (2 %, 150 kDa, TdB consultancy) was injected intravenously to visualize the
554 vasculature. In a stereotactic frame, an open cranial window was drilled and covered with an
555 artificial tears gel (Bausch&Lomb) to bridge the working distance of the water immersion
556 objective used. Images were acquired with a two-photon microscope (TRiM Scope I, LaVision

557 Biotec), equipped with an optical parametric oscillator Titan-Saphir laser combination
558 (Coherent Inc.). Image stacks of 1 x 1 x 0.5 mm volume with a step size of 2 µm were scanned
559 during the excitation of TRITC with a wavelength of 1100 nm. Line scans along single vessels
560 were performed with a scanning frequency of 800-900 Hz for one second to determine the
561 flow speed of red blood cells and the direction of blood flow. To assess arteriolar and venular
562 vessels, at least three branches of the same vascular tree were scanned to define converging
563 or diverging vessels. ImageJ software was then used to analyze vessel diameters and blood
564 cell speed after stacking the line scans.
565
566 *Object place recognition test*
567 The object place recognition (OPR) test was performed with appropriate adaptations as
568 described earlier[53]. First, mice underwent a habituation phase once per day for three days
569 during which they were placed in the center of a dimly lit (approximately 20 lux) rectangular
570 open field apparatus and left for 10 min to freely explore it. The next day, the sample trial and
571 the test trial took place. In the sample trial, two identical objects were placed in the corners
572 of the apparatus, and the mice were allowed 10 min to explore the apparatus and the objects
573 freely. Afterwards, the mice were transported back to their home cage for 60 min. During the
574 test trial, the mice were placed in the open field apparatus and allowed for five min to explore
575 the previously presented objects, with the difference being that one object was displaced. A
576 visual clue attached to the wall of the apparatus was used for the spatial orientation of the
577 mice[54]. The animals' behavior during the OPR test was recorded with a digital camera, and
578 the scoring procedure was conducted using the software ANY-maze (Stoelting Inc.). The
579 preference index was calculated as the ratio of time spent exploring the displaced object
580 divided by the total time for exploring both objects. Different combinations of objects and

581 objects' locations were used between animals and for each time point to eliminate any
582 possible biased preferences.
583
584 *Barnes maze test*
585 The Barnes maze test was performed as described previously[55] with minor adaptations. The
586 Barnes maze apparatus consisted of an elevated circular platform with 19 closed holes and
587 one open hole leading to an escape box (Stoelting Co., Cat. Nr. 60170). The mice were trained
588 to find the escape box based on visual cues placed in the surrounding environment. The
589 apparatus was brightly lit with approximately 350 lux. The mice underwent five days of
590 acquisition followed by the probe trials on days 6 and 17. During the acquisition trials, the
591 mice were placed in the middle of the apparatus and allowed to find the escape box for 3 min.
592 If the mice failed to locate or enter the escape hole in this period, they were gently guided
593 and placed inside the escape box. The mice were left inside the escape box for 1 min before
594 being transported back to the home cage. Each mouse received four acquisition trials daily
595 with an inter-trial interval of 15 min. On days 6 and 17, the escape box was removed, the hole
596 was closed, and the apparatus was turned by 180° to exclude the influence of intra-maze cues.
597 Then, mice were placed in the middle of the apparatus and allowed to explore it for 90 seconds
598 before being transported back to their home cage. The mice were recorded during acquisition
599 and probe trials, and the videos were analyzed offline using ANY-maze (Stoelting Inc.).
600
601 *Carotid artery preparation*
602 To assess the recombination in carotid arteries, the mice were perfused with 4 %
603 paraformaldehyde after Ringer perfusion under deep anesthesia. Subsequently, the region
604 where the common carotid artery diverges into the internal and the external carotid arteries

605 was prepared under a stereomicroscope. Then, a tissue block was removed and snap-frozen.
606 Cryosections (20 µm) were prepared using a cryostat (CM3050, Leica) and costained with DAPI
607 (#A1001, BioChemica, 1 µg/mL). The images were taken using a fluorescence microscope
608 (DMI6000B, Leica).
609
610 *Tissue processing for subsequent protein analyses*
611 Mice were transcardially perfused with heparin (2 or 10 IU/mL)/Ringer´s solution under deep
612 anesthesia. Brains were removed and either snap-frozen directly or post-fixed in 3.7 %
613 formalin solution at 4°C overnight. After post-fixation, the brains were washed and left for 48
614 h in a 30 % saccharose solution. Finally, the brains were snap-frozen in 2-methylbutane and
615 kept at -80°C until cryosectioning was performed.
616
617 *Immunohistochemical staining and microscopy*
618 Brains were cut with a cryotome (CM3050, Leica) at -25°C at a thickness of 20 µm and stored
619 at -20°C. For staining, the sections were permeabilized with 0.3 % Triton-X 100 for 15-30 min
620 and then blocked with 3-5 % BSA in 0.3 % Triton-X 100 for 30-75 min at room temperature.
621 Then, sections were incubated with the respective primary antibody diluted in the blocking
622 solution at 4°C overnight. Incubation with secondary antibodies took place for one hour at
623 room temperature. For collagen IV, caveolin-1, shank2, MAP2, and bassoon staining, an
624 antigen retrieval step (20 min boiling at 95°C in a 10 mM tri-sodium citrate buffer pH 6.0) was
625 included. For the MAP2 staining, a Fab fragment solution (115-007-003, Jackson
626 ImmunoResearch) was added to the blocking solution to reduce the nonspecific binding of the
627 primary antibody. The following primary antibodies were used: anti-Bassoon: #141016,
628 Synaptic Systems, 1:500; anti-Caveolin-1: #3267, Cell Signaling Technology, 1:400; anti-CD31:

629 #MCA2388, Bio-Rad, 1:200; anti-Collagen IV: #134001, Bio-Rad, 1:200; anti-GFAP: #AB5541,
630 Millipore, 1:400; anti-Iba1: #019-19741, FUJIFILM Wako, 1:400; anti-MAP2: #MA1-25044,
631 Thermo Fischer Scientific, 1:500; anti-MBP: #MAB386, Millipore, 1:250; anti-NeuN: #MAB377,
632 Millipore, 1:500; anti-Shank2: #162204, Synaptic Systems, 1:500.
633 The following secondary antibodies were used: anti-chicken Alexa Fluor 488: #ab150169,
634 Abcam, 1:200; anti-goat Alexa Fluor 488: #A11055, Thermo Fischer Scientific, 1:200; anti-goat
635 Alexa Fluor 555: #A21432, Thermo Fischer Scientific, 1:400; anti-guinea pig Alexa Fluor 633:
636 #A21105, Thermo Fischer Scientific, 1:400; anti-mouse Cy3: #715-165-151, Jackson
637 ImmunoResearch, 1:400; anti-mouse Alexa Fluor 555: #A21422, Thermo Fischer Scientific,
638 1:400; anti-rabbit Alexa Fluor 750: #A21039, Thermo Fischer Scientific, 1:400; anti-rat Alexa
639 Fluor 647: #ab150155, Abcam, 1:400.
640 The images were acquired using the fluorescence microscopes Leica DMI6000B and Leica
641 Stellaris 5. Analyses were performed in a blinded manner using ImageJ (National Institutes of
642 Health). String vessels were identified as structures positively stained for the basement
643 membrane component collagen IV and negatively stained for an endothelial marker as
644 described earlier[56].
645
646 *Immunoblotting*
647 Hippocampal and cortical tissue samples were prepared by cutting the respective brain
648 regions from frozen brains in the cryotome. Tissue was lysed, and the protein content was
649 determined using a Lowry assay. Samples were supplemented 1:4 with SDS buffer (0.75 M
650 Tris-HCl, 0.08 g ml−1 SDS, 40% glycerol, 0.4 mg ml−1 bromophenol blue, and 62 mg ml−1 DTT)
651 and incubated at 95 °C for 10 min. After loading on SDS–PAGE gels, proteins were transferred
652 to nitrocellulose membranes, which were then incubated with primary antibodies overnight

653 at 4°C. Afterwards, the membranes were incubated with HRP-conjugated secondary
654 antibodies for two hours at room temperature. For detection, enhanced chemiluminescence
655 (SuperSignal West Femto Substrate, Thermo Scientific) and a digital detection system (Fusion
656 Solo S, Vilber) were used. Immunoblots were analyzed by the detection software or ImageJ
657 (National Institutes of Health. The following antibodies were used: anti-pTau (Ser202/Thr205)
658 AT8: #MN1020, Thermo Fischer Scientific, 1:1000; anti-pTau (Thr231) AT180: #MN1040,
659 Thermo Fischer Scientific, 1:500; anti-Tau: #4019S, Cell Signaling Technologies, 1:1000; anti-
660 Actin: #MAB1501, Millipore, 1:2500; anti-Albumin: #A90-134. Bethyl Laboratories, 1:16.000;
661 anti-VEGFR2 55B11: #2479, Cell Signaling Technology, 1:1000; anti-mouse HRP: #P0447, DAKO
662 Cytomation, 1:2500; anti-rabbit HRP: #P0448, DAKO Cytomation, 1:2500; anti-goat HRP:
663 #P0160, DAKO Cytomation, 1:2500.
664
665 *VEGF measurement*
666 The concentration of VEGF was determined in blood collected from the heart of deeply
667 anesthetized mice. After centrifuging at 16,400*g* and 4 °C for 5 min, EDTA plasma was stored
668 at −80 °C before measurement. The amount of VEGF was determined by using a commercially
669 available ELISA kit (RAB0509, Sigma-Aldrich) according to the manufacturer's protocol.
670
671 *Statistics*
672 No statistical methods were used to predetermine sample sizes, but our sample sizes are
673 similar to those reported in previous publications[17,27,56]. All the values are expressed as means
674 ± SEM. Analyses were performed using GraphPad Prism 8. Data values were assessed for
675 normality and equality of variances. If the raw data did not meet these criteria, a non-
676 parametric method was applied. Two groups were compared using a two-tailed, unpaired,

677 parametric Student's t-test or Mann-Whitney test. For multiple comparisons, we used one- or
678 two-way ANOVA as stated in the figure legends. Post-hoc tests were only performed if the
679 ANOVA test showed a significant difference. Survival was tested using the Log-rank (Mantel-
680 Cox) test. Differences were considered to be significant at $P < 0.05$.

681 FIGURES

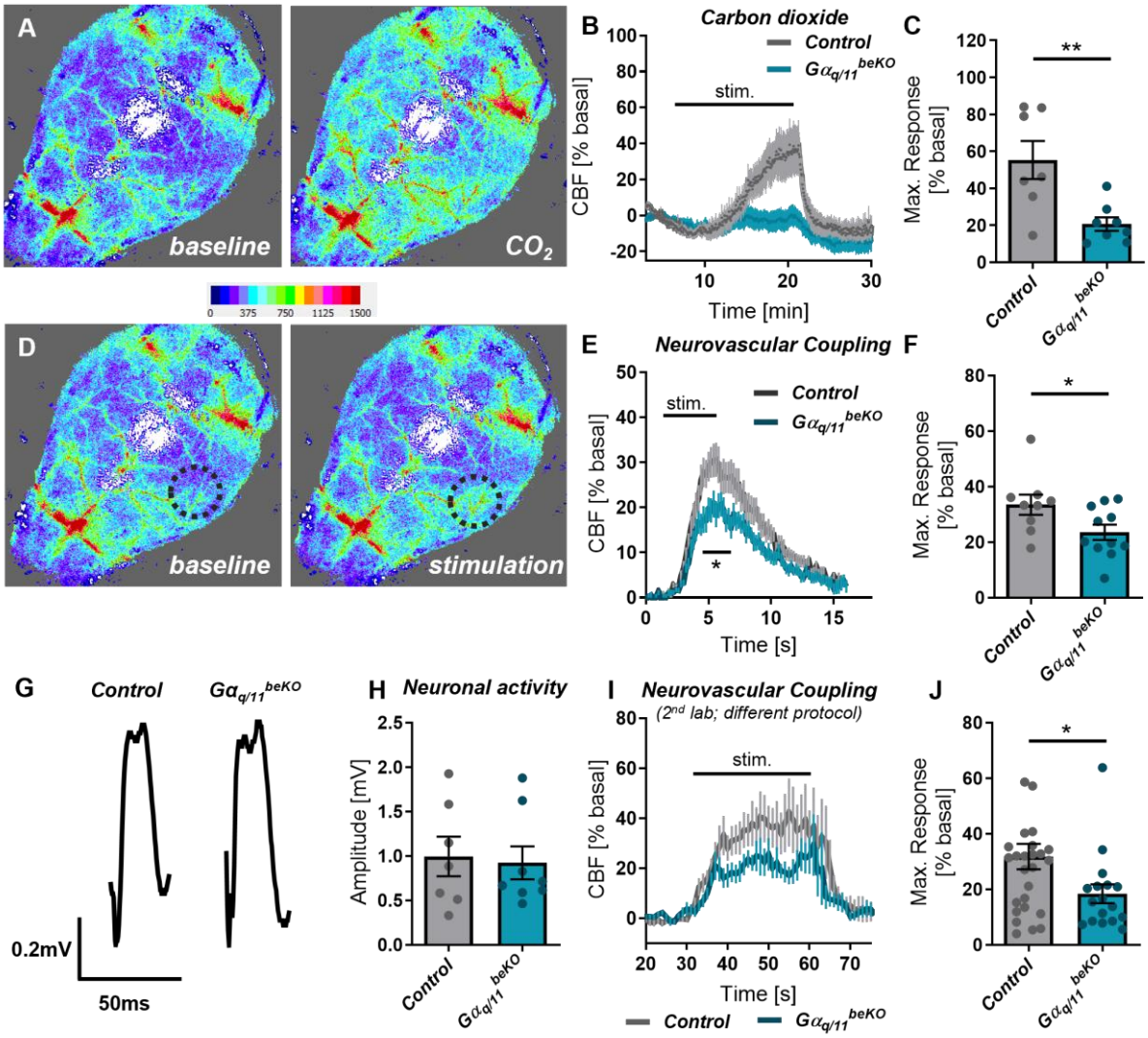

682
683 ***Figure 1: Brain endothelial Gα$_{q/11}$ signaling mediates cerebrovascular reactivity to CO_2 and***
684 ***neuronal activity.*** (**A**) Representative images of perfusion measurements using laser speckle
685 imaging before and during CO_2 exposure. (**B**) Time course of cerebral blood flow (CBF) during
686 CO_2 exposure in ventilated, ketamine/xylazine-anesthetized Gα$_{q/11}^{beKO}$ and control mice. N=7-
687 8. (**C**) Maximal CBF response of curves shown in (B). Mann-Whitney test. (**D**) Representative
688 images of perfusion measurements using laser speckle imaging before and during whisker pad
689 stimulation. Black circle indicates the analyzed area above the somatosensory cortex. (**E**) Time
690 course of cerebral blood flow (CBF) during whisker pad stimulation in ventilated,
691 ketamine/xylazine-anesthetized Gα$_{q/11}^{beKO}$ and control mice. N=9-11; *p<0.05 in Sidak´s post-
692 test after two-way-ANOVA. (**F**) Maximal CBF response of curves shown in (E). Mann-Whitney
693 test. (**G**) Representative traces of local field potentials measured in Gα$_{q/11}^{beKO}$ and control mice
694 during whisker pad stimulation. (**H**) Mean amplitudes of local field potentials measured in
695 Gα$_{q/11}^{beKO}$ and control mice. (**I**) Time course of CBF measured by laser Doppler flowmetry
696 during whisker pad stimulation in spontaneously breathing, isoflurane-anesthetized Gα$_{q/11}^{beKO}$
697 and control mice. N=17-27 recordings of 6-9 mice. (**J**) Maximal CBF response of curves shown
698 in (I). Mann-Whitney test. Shown are means±SEM. *p<0.05. **p<0.01.

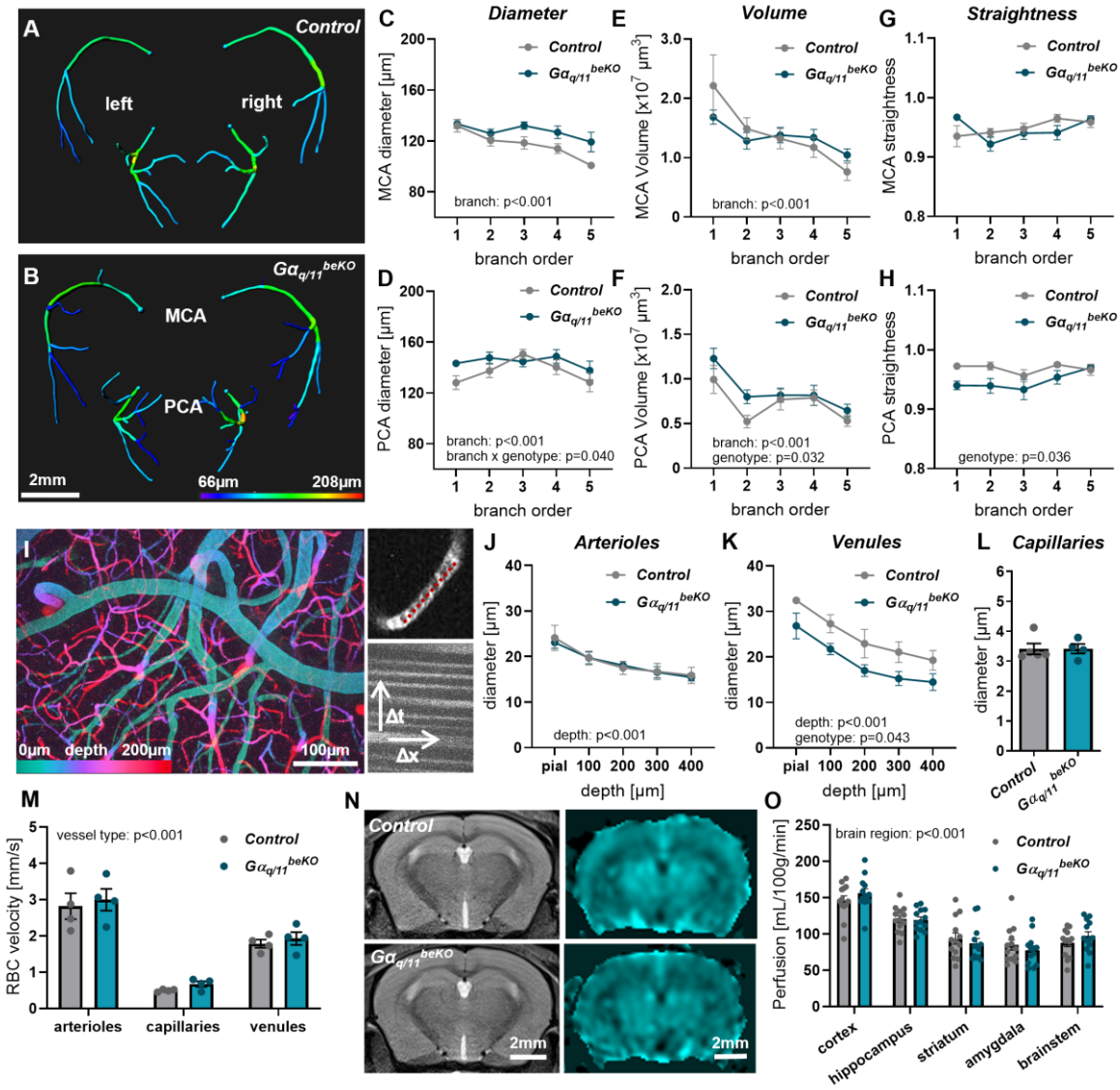

Figure 2: Gα$_{q/11}^{beKO}$ mice do not show structural or functional vascular alterations at baseline. (**A**, **B**) Representative images of reconstructed middle and posterior cerebral artery branches (MCA, PCA) from time-of-flight (TOF) angiography measurements in control (A) and Gα$_{q/11}^{beKO}$ (B) mice. Color-coding indicates diameter of the respective vessel segment. See Extended Figure 2 for detailed reconstruction processing. (**C-H**) Quantifications of diameter, volume, and straightness of vascular branches of MCAs and PCAs of control and Gα$_{q/11}^{beKO}$ mice. Branch order 1 refers to the first segment originating from the Circle of Willis. Means of left and right arteries are shown. N=8-14. Two-way ANOVA, significantly different variables are indicated in the graphs. (**I**) Maximum intensity projection of a volume taken by two-photon microscopy is shown (left side). Tissue depth is color-coded. Right upper panel: a single capillary filled with blood cells (dark gaps) is shown. Red line indicates a line scan to measure red blood cell (RBC) velocity. Stacking of line scans enables determination of velocity by taking the length of the line and the frequency of the scanning into account (right lower panel). (**J-L**) Diameter of penetrating arterioles (J), ascending venules (K), and capillaries (L) of control and Gα$_{q/11}^{beKO}$ mice are shown. N=4-5. Two-way ANOVA (J, K), significantly different variables are indicated in the graphs. (**M**) Quantification of RBC velocities in different parts of the vascular tree of control and Gα$_{q/11}^{beKO}$ mice is shown. N=4. Two-way ANOVA, significantly different variable is indicated in the graph. (**N**) Representative images of T2-weighted magnetic

718 resonance imaging (MRI) and arterial spin labeling (ASL) MRI of control and $G\alpha_{q/11}^{beKO}$ mice
719 are shown. T2 images were used to define regions to be analyzed in the ASL images. (**O**)
720 Quantification of ASL signals in different brain regions of control and $G\alpha_{q/11}^{beKO}$ mice are
721 shown. N=13. Two-way ANOVA, significantly different variable is indicated in the graph.
722 Shown are means±SEM.
723

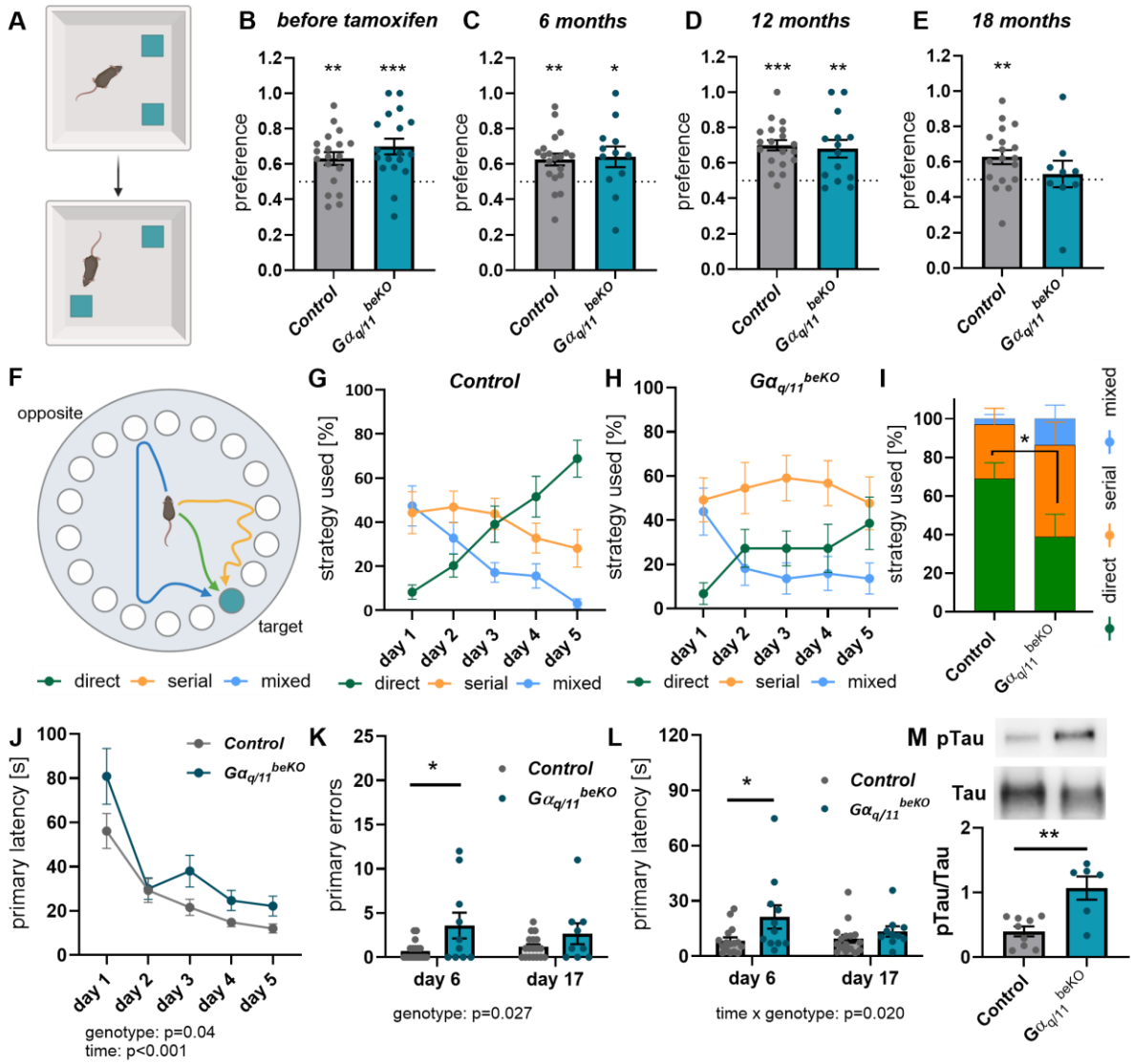

Figure 3: Loss of brain endothelial Gα$_{q/11}$ signaling leads to mild cognitive impairment in aged mice. (**A**) Scheme of object place recognition (OPR) test with the upper part showing the situation before and the lower part showing the situation after moving one of the two objects. (**B-E**) OPR preference indices at different time points are shown. Tamoxifen was administered at the age of 7-8 weeks to control and Gα$_{q/11}^{beKO}$ mice to induce genetic deletion. Time points indicate the age of the mice. Dotted lines mark chance level (0.5), and Student´s *t*-tests were applied to test against chance level. N=9-18. (**F**) Scheme of Barnes maze test is shown with different colors indicating different strategies to find the target hole. (**G**, **F**) The proportion of different strategies on the training days is shown for control (G, N=16) and Gα$_{q/11}^{beKO}$ (H, N=11) mice. (**I**) Comparison of strategies used on day 5 of the training between control and Gα$_{q/11}^{beKO}$ mice. N=11-16. Two-way ANOVA followed by Sidak's posthoc test, strategy: p<0.001, genotype x strategy: p<0.001. (**J**) Primary latency until the target hole was found during the training days is shown for control and Gα$_{q/11}^{beKO}$ mice. N=11-16. Two-way ANOVA, significantly different variables are indicated in the graph. (**K**, **L**) Primary errors (K) and primary latency (L) on test days 6 and 17 are shown for control and Gα$_{q/11}^{beKO}$ mice. N=11-16, mixed effect analysis for repeated measurements followed by Sidak's posthoc test, significantly different variables are indicated in the graph. (**M**) Representative Western blots and quantification of phosphorylated (AT8, pSer202/pThr205) and full tau in hippocampal tissue of control and Gα$_{q/11}^{beKO}$ mice are shown. Mann-Whitney test. Mean±SEM. *p<0.05, **p<0.01, ***p<0.001.

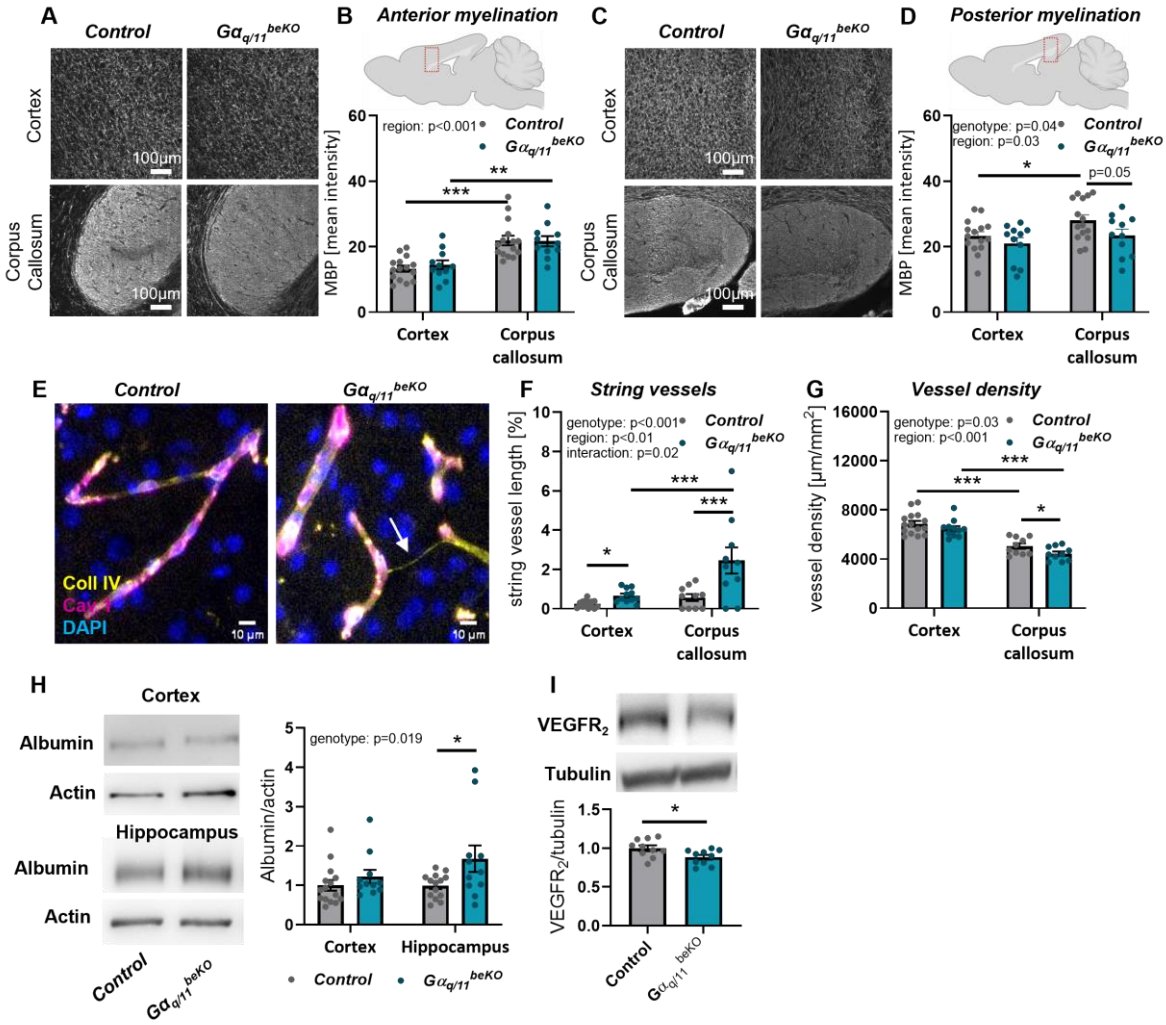

Figure 4: Aged Gα$_{q/11}^{beKO}$ mice show vascular and structural alterations in the white matter of the brain. (**A**) Representative images of myelin basic protein (MBP) in anterior cortex and corpus callosum of control and Gα$_{q/11}^{beKO}$ mice are shown. (**B**) Upper illustration indicates the area of imaging and lower part shows the quantification of MBP intensities in respective areas of aged control and Gα$_{q/11}^{beKO}$ mice. N=10. Two-way ANOVA followed by Sidak's posthoc test, significantly different variable is indicated in the graph. (**C**) Representative images of myelin basic protein (MBP) in posterior cortex and corpus callosum of control and *Gα$_{q/11}^{beKO}$* mice are shown. (**D**) Upper illustration indicates the area of imaging and lower part shows the quantification of MBP intensities in respective areas of aged control and *Gα$_{q/11}^{beKO}$* mice. N=10. Two-way ANOVA followed by Sidak's posthoc test, significantly different variable is indicated in the graph. (**E**) Representative images of staining for endothelial cells (caveolin 1, Cav 1) and basement membranes (collagen IV, Coll IV) in the cortex of control and Gα$_{q/11}^{beKO}$ mice are shown. Arrow indicates a string vessel, an empty basement membrane tube, indicating loss of endothelial cells. (**F**, **G**) Quantification of string vessels (F) and vessel density (G) in cortex and corpus callosum of aged control and Gα$_{q/11}^{beKO}$ mice. N=10-15 Two-way ANOVA followed by Sidak's posthoc test, significantly different variables are indicated in the graph. (**H**) Representative images and quantification of Western blots of albumin in cortical and hippocampal brain tissue of aged control and *Gα$_{q/11}^{beKO}$* mice. N=11-15 Two-way ANOVA followed by Sidak's posthoc test, significantly different variable is indicated in the graph. (**I**) Representative images and quantification of Western blots of VEGFR$_2$ in cortical brain tissue

765 of aged control and $G\alpha_{q/11}^{beKO}$ mice. Student´s *t*-test. N=10. Mean±SEM. *p<0.05, **p<0.01,
766 ***p<0.001.

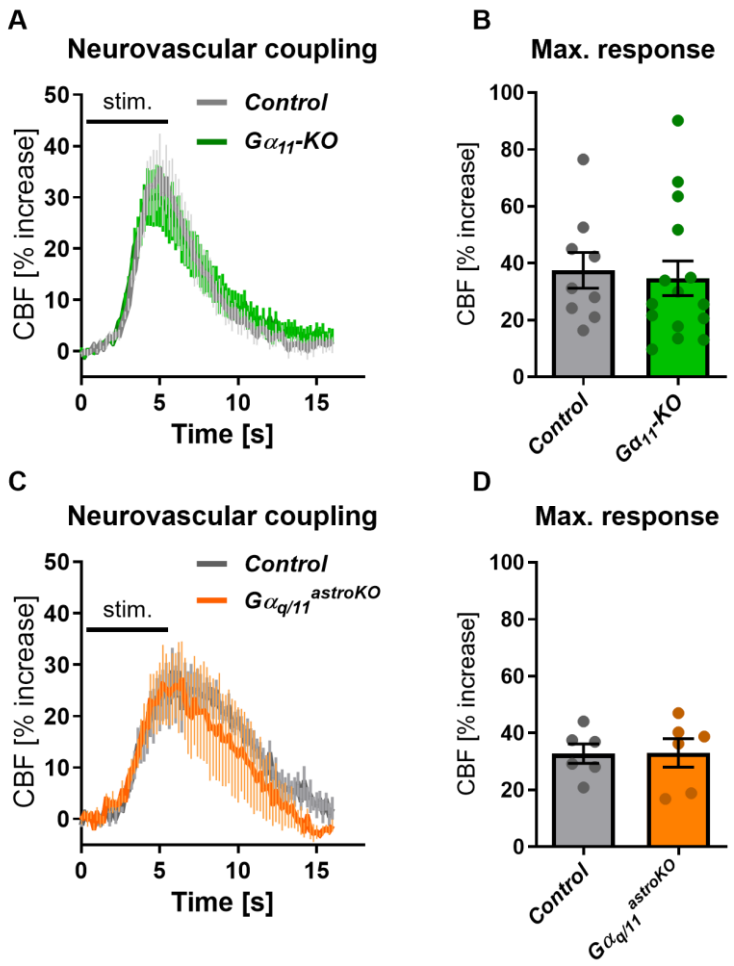

Extended Figure 1: Whole genome deletion of Gna11 or astrocytic deletion of the Gα$_{q/11}$ signaling pathway does not affect neurovascular coupling. (**A**) Time course of cerebral blood flow (CBF) recording during whisker pad stimulation in Gα$_{11}$-*KO* and control mice. N=9-15. (**B**) Maximal CBF response of curves shown in (A). (**C**) Time course of CBF recording during whisker pad stimulation in Gα$_{q/11}^{astroKO}$ and control mice. N=6. (**B**) Maximal CBF response of curves shown in (C). Mean±SEM.

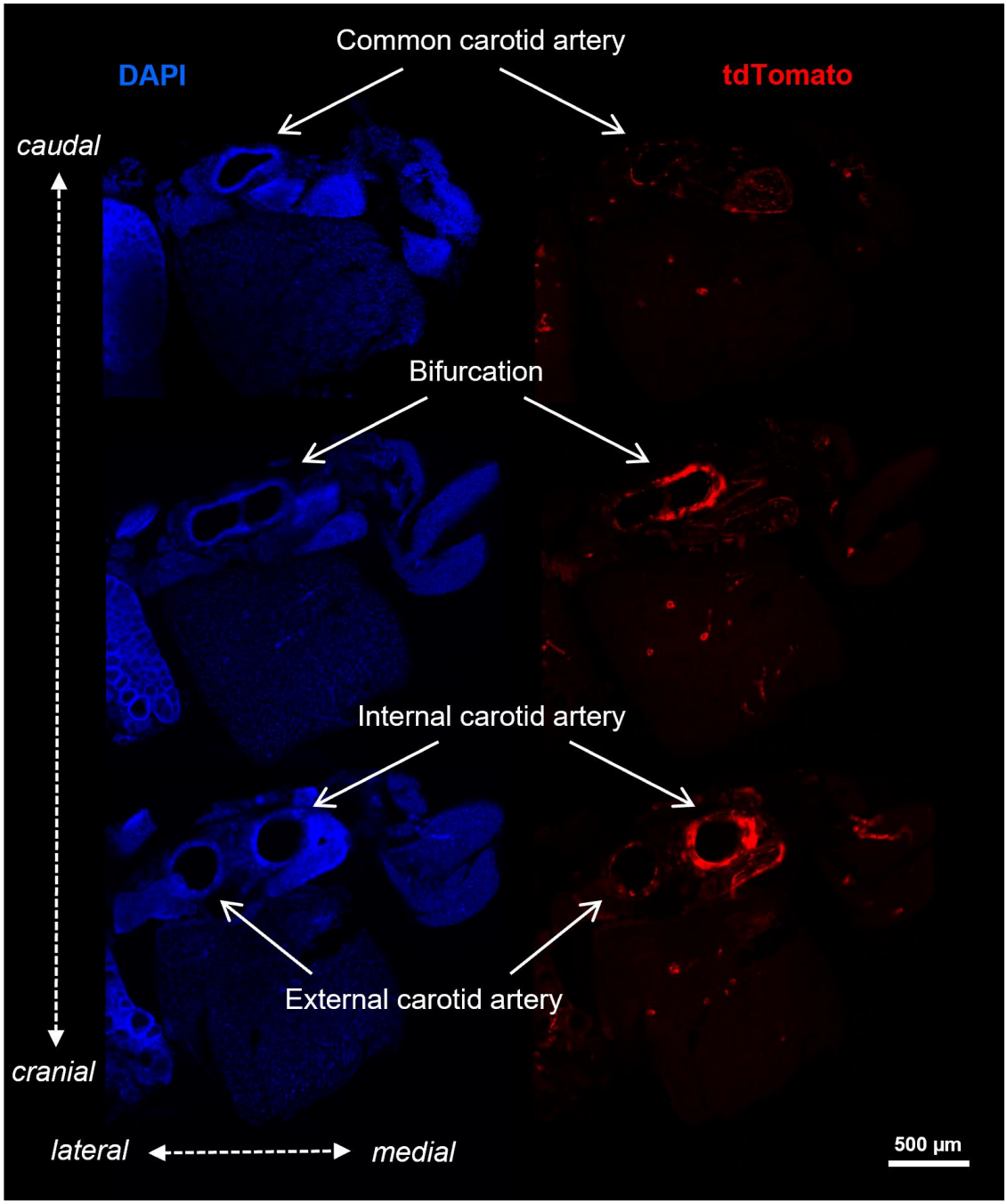

774
775
776 ***Extended Figure 2: Recombination of the Slco1c1-CreER^{T2} mouse line starts at the bifurcation***
777 ***between the internal and external carotid arteries.*** Shown are three different cross-sections
778 of tissue in the region where the common carotid artery diverges into the internal and the
779 external carotid arteries. A *Slco1c1-CreER^{T2}*; *Ai14$^{flx/flx}$* mouse, two weeks after the start of
780 tamoxifen injection, was used. TdTomato indicates recombination, and DAPI was used to
781 counterstain the tissue.

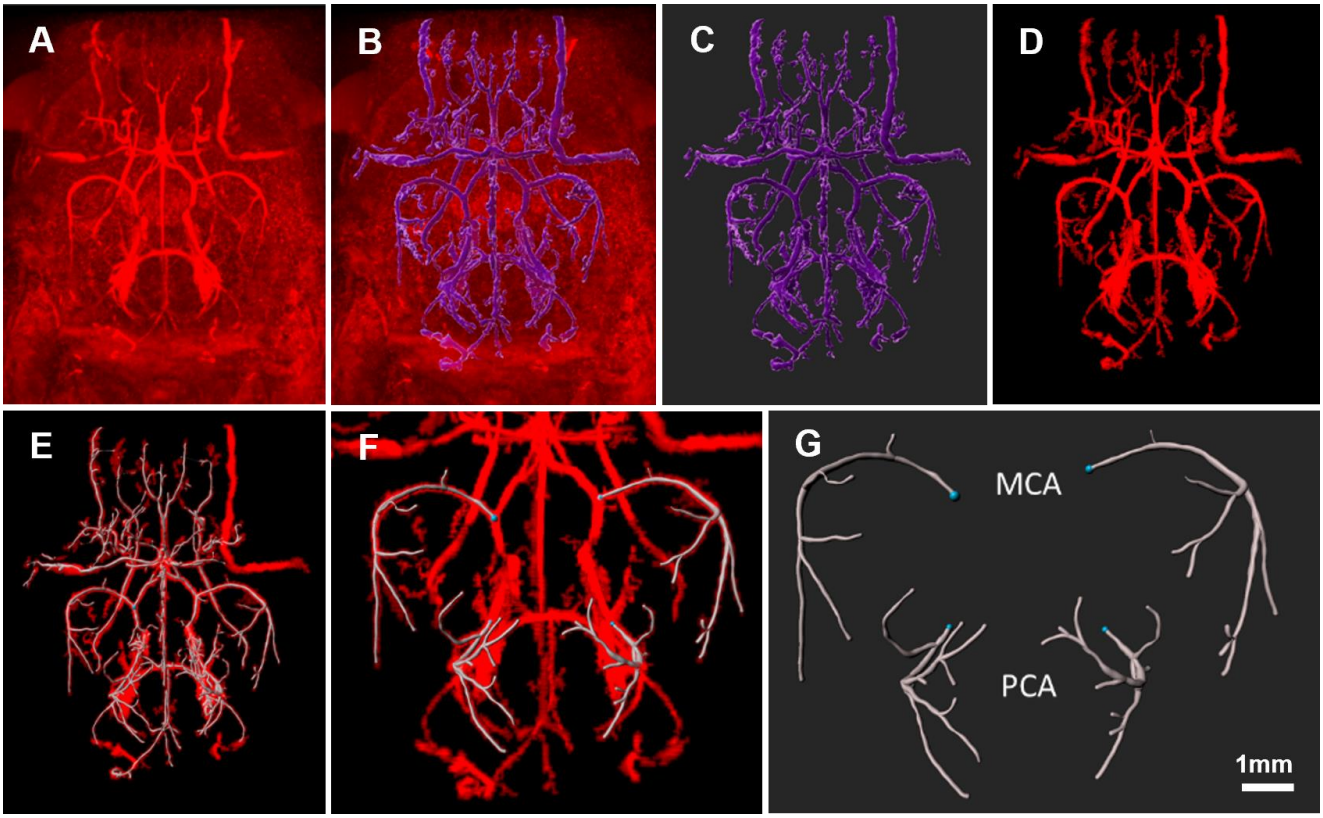

Extended Figure 3: Workflow for processing TOF angiography data sets. An example of a data set obtained by time of flight (TOF) angiography MRI and its processing using the software Imaris is shown. (**A**) original data set, (**B**) surface creation overlay, (**C**) final surface creation after removing noise, (**D**) mask of the surface creation, (**E**) filaments detection, (**F**) magnification of (E) and selection of middle cerebral arteries (MCA) and posterior cerebral arteries (PCA) with the starting points (blue dots) at the circle of Willis. (**G**) shown are the final filaments used for quantification (see main Figure 2).

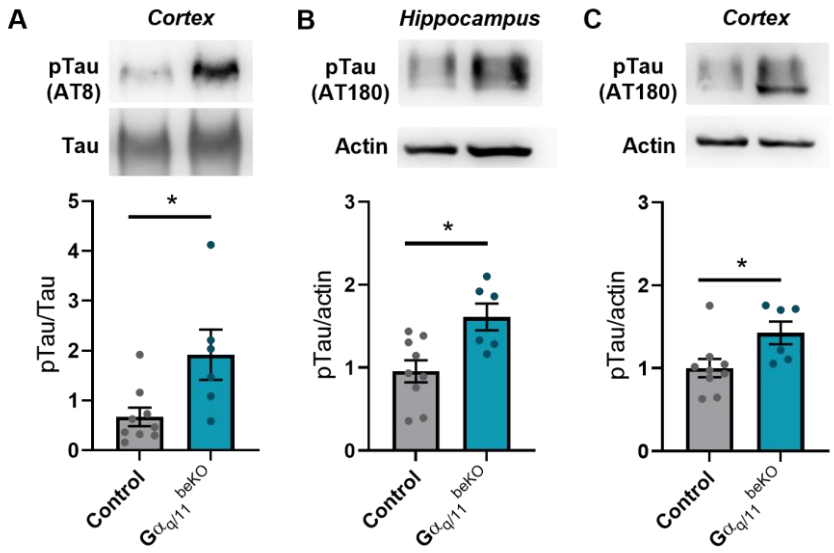

Extended Figure 4: Increased phosphorylation of tau in brains of $G\alpha_{q/11}^{beKO}$ mice. (**A**) Representative Western blots and quantification of phosphorylated (AT8, pSer202/pThr205) and full tau in cortical tissue of control and $G\alpha_{q/11}^{beKO}$ mice are shown. (**B**, **C**) Representative Western blots and quantification of phosphorylated (AT180, pThr231) and actin in hippocampal (B) and cortical (C) tissue of control and $G\alpha_{q/11}^{beKO}$ mice are shown. Mean±SEM. N=6-8, Mann-Whitney test, *p<0.05.

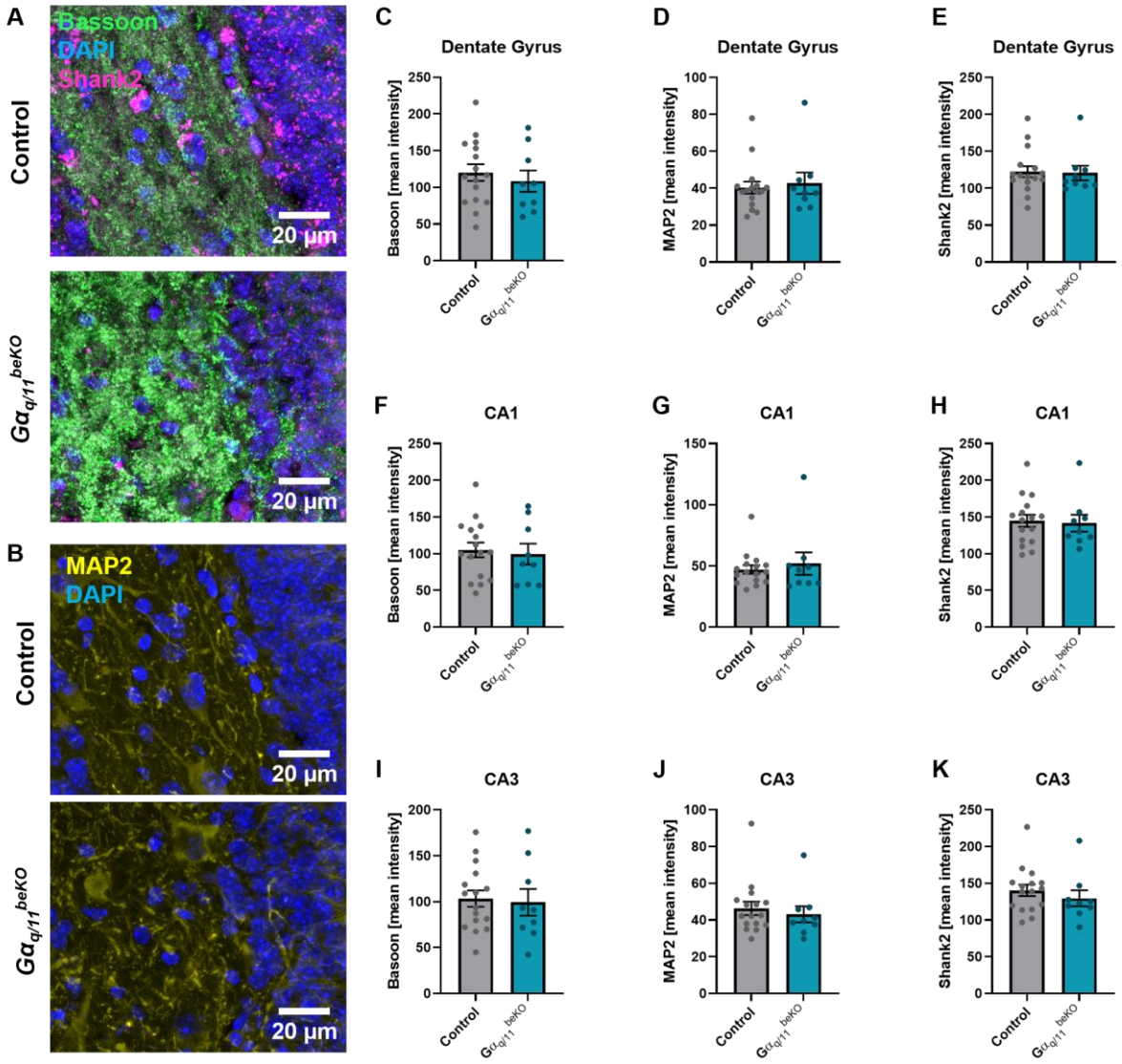

Extended Figure 5: No difference in neuronal markers in hippocampal subregions of aged Gα$_{q/11}^{beKO}$ mice. (**A**, **B**) Representative images of staining for synaptic markers bassoon and shank2 (A) and structural marker MAP2 (B) in hippocampal tissue of control and Gα$_{q/11}^{beKO}$ mice. (**C-K**) Quantification of mean intensities of bassoon (C, F, I), MAP2 (D, G, J), and Shank2 (E, H, K) are shown for the hippocampal regions dentate gyrus (C-E), CA1 (F-H), and CA3 (I-K) in aged control and *Gα$_{q/11}^{beKO}$* mice are shown. Mean±SEM.

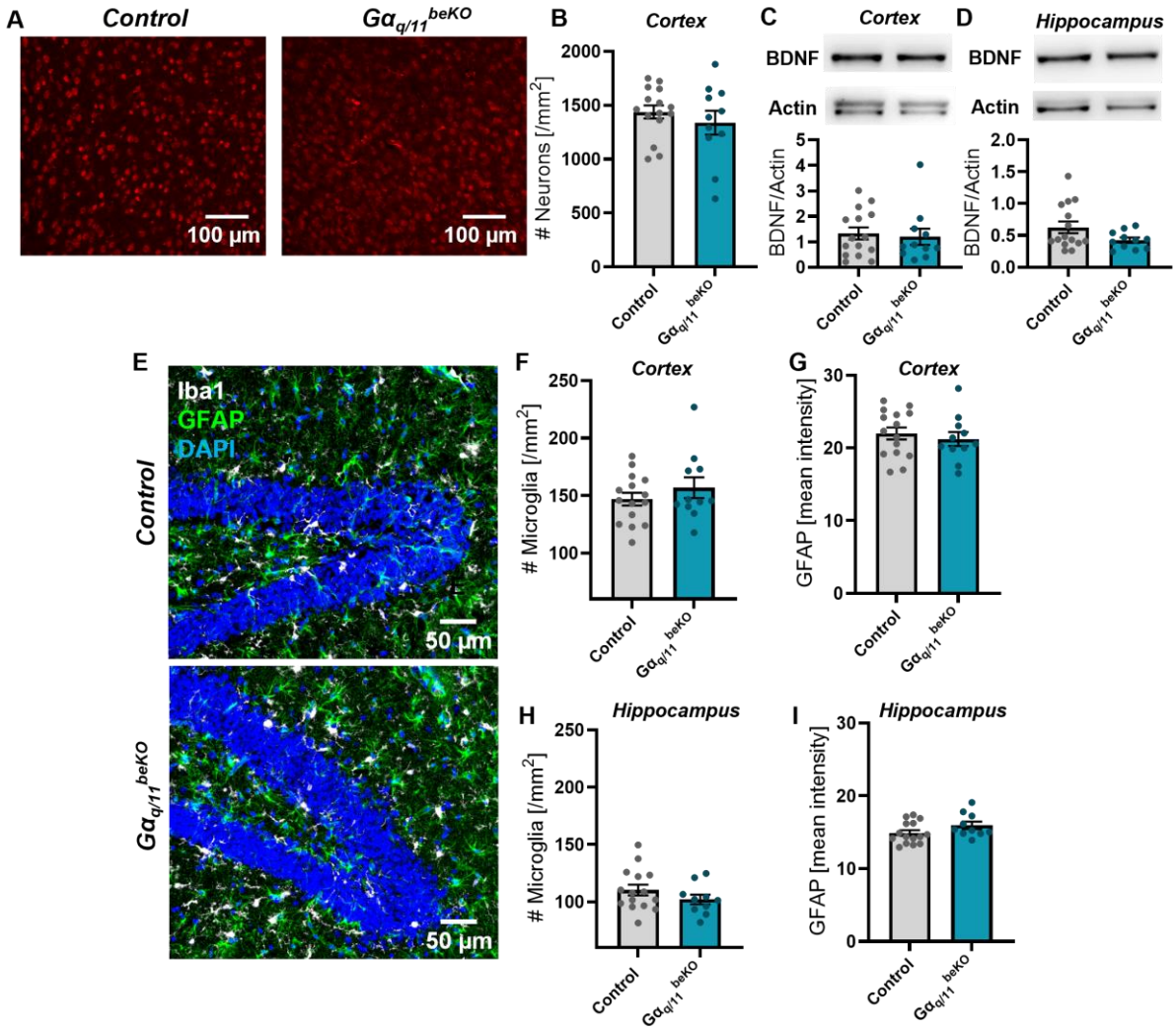

Extended Figure 6: No difference in the number of neurons or neuroinflammatory markers in brains of aged Gα$_{q/11}^{beKO}$ mice. (**A**, **B**) Representative images (A) and quantification (B) of neuronal marker NeuN in cortex of aged control and Gα$_{q/11}^{beKO}$ mice. (**C**, **D**) Representative Western blots and quantification of brain-derived neurotrophic factor (BDNF) and actin in cortical (C) and hippocampal (D) tissue of aged control and Gα$_{q/11}^{beKO}$ mice are shown. (**C-G**) Representative images (C) and quantification (D-G) of microglia (Iba1; D, F) and astrocytic activation (GFAP, E, G) in cortical (D, E) and hippocampal (C, F, G) tissue of aged control and Gα$_{q/11}^{beKO}$ mice. N=10-15. Mean±SEM.

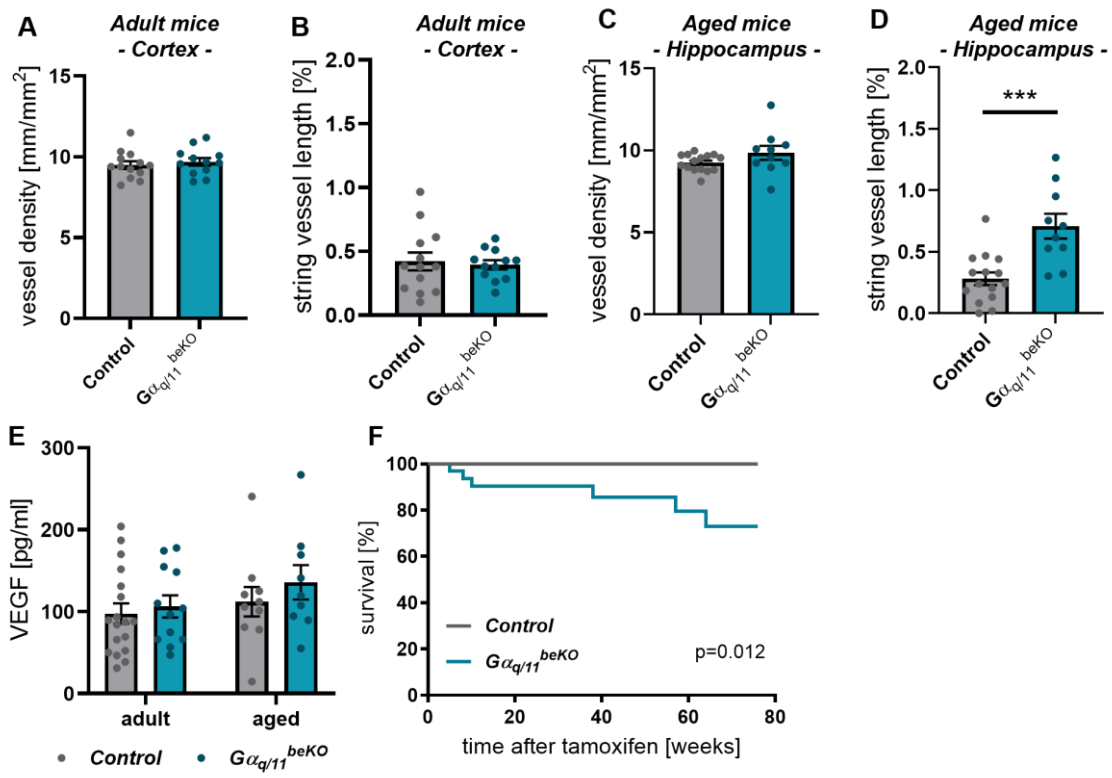

Extended Figure 7: Vessel density, string vessels, VEGF, and mortality in $G\alpha_{q/11}^{beKO}$ mice. (**A, B**) Vessel density (A) and string vessel (B) quantification in the cortex of adult control and $G\alpha_{q/11}^{beKO}$ mice. N=12-13. (**C, D**) Vessel density (C) and string vessel (D) quantification in the hippocampus of aged control and $G\alpha_{q/11}^{beKO}$ mice. N=10-15. Student´s t test. ***p<0.001. (**E**) Quantification of VEGF concentration in plasma of adult and aged control and $G\alpha_{q/11}^{beKO}$ mice. N=9-18. (**F**) Survival curve of control and $G\alpha_{q/11}^{beKO}$ mice. Tamoxifen was administered at the age of 7-8 weeks. N=28-31. Log-rank (Mantel-Cox) test. Mean±SEM.